communications physics

Article

https://doi.org/10.1038/s42005-024-01887-0

Built-in Bernal gap in large-angle-twisted monolayer-bilayer graphene

Check for updates

Alex Boschi[1], Zewdu M. Gebeyehu[1,2], Sergey Slizovskiy[3,4], Vaidotas Mišeikis[1,2], Stiven Forti[1,2], Antonio Rossi[1,2], Kenji Watanabe[5], Takashi Taniguchi[6], Fabio Beltram[7], Vladimir I. Fal'ko[3,4,8], Camilla Coletti[1,2] ✉ & Sergio Pezzini[7] ✉

Atomically thin materials offer multiple opportunities for layer-by-layer control of their electronic properties. While monolayer graphene (MLG) is a zero-gap system, Bernal-stacked bilayer graphene (BLG) acquires a finite band gap when the symmetry between the layers' potential energy is broken, usually, via a displacement electric field applied in double-gate devices. Here, we introduce a twistronic stack comprising both MLG and BLG, synthesized via chemical vapor deposition, showing a Bernal gap in the absence of external fields. Although a large (~30°) twist angle decouples the MLG and BLG electronic bands near Fermi level, proximity-induced energy shifts in the outermost layers result in a built-in asymmetry, which requires a displacement field of 0.14 V/nm to be compensated. The latter corresponds to a ~10 meV intrinsic BLG gap, a value confirmed by our thermal-activation measurements. The present results highlight the role of structural asymmetry and encapsulating environment, expanding the engineering toolbox for monolithically-grown graphene multilayers.

The electronic properties of few-layer graphenes are sensitive to layer number[1], stacking order[2,3], lack or presence of inversion symmetry[4,5], external electromagnetic fields[6], as well as to the twist angle between consecutive layers (their relative crystallographic orientations)[7]. Based on this last tuning parameter, the band hybridization between contiguous sheets can be artificially modulated, resulting in spectacular emergent behaviors for small-angle values associated to specific periodicities of the interlayer moiré[8]. This paradigm, initially demonstrated in twisted bilayer graphene (TBG)[9,10], has now been extended to a plethora of related moiré systems[11], including twisted MLG-BLG (TMBG). For twist angles ~1°, TMBG has been shown to support flat bands promoting correlated and topological phases, including insulators[12,13], orbital magnets[14–16] and charge density waves[17]. The lack of inversion symmetry makes the electronic response of small-angle TMBG strongly dependent on the direction of an external displacement field (D) that can be controlled by top and bottom gate electrodes[12–15,17]. In the limit of large twist angle (where moiré effects are negligible), TMBG is expected to decompose into two low-energy subsystems that retain unperturbed MLG and BLG character, mimicking the independent-MLGs behavior found in large-angle TBG[18–23]. However, a complete picture of large-angle TMBG needs to account for its structural asymmetry, which can have a subtle (yet measurable) influence on the exact band structure close to Fermi level. Specifically, not only BLG is sensitive to D – which drives band-gap opening[24–26] exploitable for quantum confinement[27–29] and multiple phase transitions[30–32] – but also, when embedded in stacks, to environment-induced interlayer asymmetry[5,24], as demonstrated by the observation of a mini-gap in large-angle-twisted double BLG (TDBG)[33]. Building on these findings, Agarwal et al. recently reported optoelectronic properties widely beyond the independent-subsystems scenario of TDBG[34]. These results motivate further exploration of BLG-containing stacks – such as large-angle TMBG – as well as the development of scalable synthesis methods for these systems – such as chemical vapor deposition (CVD) growth of single crystals[35].

In this work, we provide experimental evidence (supported by detailed mesoscale modelling) for a built-in band gap in a BLG studied as a part of an hBN-encapsulated large-angle TMBG. Key to our observations is the ability to directly grow monolithic TMBG crystals via low-pressure CVD (LP-CVD) and integrate them into high-quality van der Waals (vdW) devices.

[1]Center for Nanotechnology Innovation @NEST, Istituto Italiano di Tecnologia, Piazza San Silvestro 12, I-56127 Pisa, Italy. [2]Graphene Labs, Istituto Italiano di Tecnologia, Via Morego 30, 16163 Genova, Italy. [3]National Graphene Institute, The University of Manchester, Manchester, M13 9PL, UK. [4]School of Physics & Astronomy, The University of Manchester, Oxford Rd., Manchester, M13 9PL, UK. [5]Research Center for Electronic and Optical Materials, National Institute for Materials Science, 1-1 Namiki, Tsukuba, 305-0044, Japan. [6]Research Center for Materials Nanoarchitectonics, National Institute for Materials Science, 1-1 Namiki, Tsukuba, 305-0044, Japan. [7]NEST, Istituto Nanoscienze-CNR and Scuola Normale Superiore, Piazza San Silvestro 12, I-56127 Pisa, Italy. [8]Henry Royce Institute for Advanced Materials, Manchester, M13 9PL, UK. ✉e-mail: camilla.coletti@iit.it; sergio.pezzini@nano.cnr.it

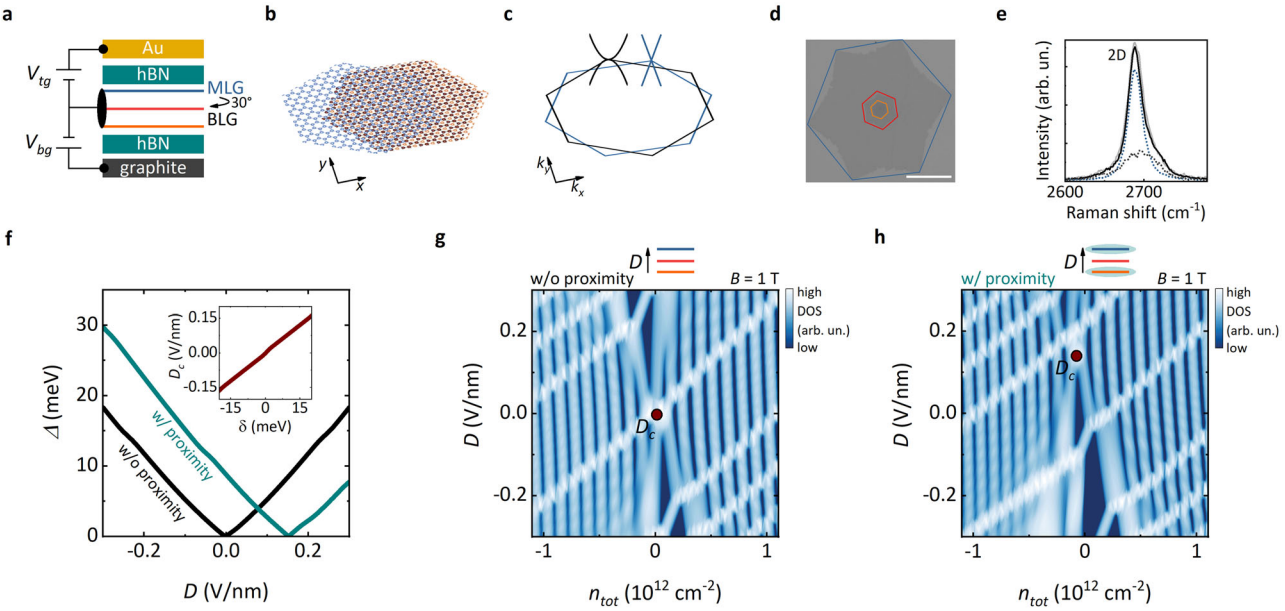

Fig. 1 | Device concept, CVD-grown twisted graphene crystals and effect of proximity energy shifts. a Side-view sketch of the studied devices. The gating scheme is indicated on the lefthand side. The three graphene layers are represented, from top to bottom, as a blue, red and orange line. **b** Real-space arrangement of the TMBG crystals: MLG (blue lattice) is superimposed to BLG (red and orange lattices, following the color scheme of panel (**a**)) with a 30° twist angle. **c** Sketch of the reciprocal-space configuration, with the MLG (blue) and BLG (black) Brillouin zones and low-energy bands at K. **d** Optical microscopy image of a representative CVD-grown trilayer graphene crystal transferred on SiO_2/Si. The three hexagons mark the concentric graphene layers forming TMBG (the color scheme follows panel (**a**)). The scale bar is 40 μm. **e** 2D Raman mode measured on TMBG on SiO_2/Si (black). The grey continuous curve is the sum of a MLG-like (dotted blue line) and a BLG (dotted grey line) component. **f** BLG band gap as a function of displacement field, without including proximity energy shifts (δ = 0, black line), and considering the shifts (δ = 18 meV, dark cyan line). Inset: gap-closing displacement field as a function of δ. (**g**, **h**) DOS of TMBG at B = 1 T calculated without including proximity energy shifts (δ = 0) (**g**) and considering the shifts (δ = 18 meV) (**h**). The dark red circle indicates the BLG gap closing. The sketch above each graph shows the TMBG layers (following the color scheme of panel (**a**)), the arrow indicates the direction of positive D-field. Dark cyan shadows highlight the graphene layers interfacing encapsulating hBN, hence affected by δ.

Results and discussion

A side-view sketch of the studied devices is shown in Fig. 1a. We employ a dual-gate configuration to perform transport measurements with independent control of gate-induced charge density (n_{tot}) and D (defined in Methods; optical microscopy images of the two TMBG devices investigated are shown in Supplementary Note 1, Figure S1). The trilayer graphene structure, encapsulated in hexagonal boron nitride (hBN), can be separated into a MLG (blue) rotated by ~30° with respect to two aligned layers forming a BLG (red and orange). In analogy with 30°-TBG[21], we expect the lattices of the two subsystems to arrange into an incommensurate configuration lacking translational symmetry (i.e., with no moiré superlattice), as sketched in Fig. 1b. The real-space twist leads to a large momentum mismatch between the MLG and BLG bands located at the Brillouin zone corners (see Fig. 1c), effectively leading to their decoupling at low energy. Based on previous results for 30°-TBG, the features of real-space quasicrystalline registry could appear only at high energies (few eV)[36,37], inaccessible in solid-state transport devices. The TMBG crystals are synthesized via the LP-CVD process introduced for 30°-TBG in ref. 21, in which the graphene-Cu interaction locks the possible interlayer twist angles to either 0° or 30°[38], with increased growth times (here, 60 min) favoring the formation of concentric multilayer structures, sharing a single nucleation point (see Methods for experimental details). In these samples, the hexagonal shape of the layers reflects their relative crystallographic orientation, making TMBG easily recognizable after transfer to SiO_2/Si substrates (see Fig. 1d) among other crystals with varied 0° or 30° rotation and layer number. Our growth approach replaces the tear-and-stack procedure ubiquitously employed for twisted graphene devices[39,40], including small-angle TMBG[12–16] and large-angle TDBG[33,34], highlighting a possible path towards scalability of this class of materials.

A first experimental indication of the composite MLG-BLG band structure of our TMBG[41] is obtained from the 2D Raman mode, which couples to the electronic degrees of freedom in graphene multilayers[42]. As shown in Fig. 1e (black continuous line), we observe a narrow peak centered at ~2690 cm^{-1} with two asymmetric shoulders, suggesting the convolution of a single-Lorentzian peak (resulting from the Dirac dispersion of MLG) with a broad multi-Lorentzian peak (resulting from the four-band parabolic dispersion of BLG). The measured TMBG 2D mode can be quantitatively reconstructed as the sum (grey continuous line) of two Raman spectra separately acquired on 30°-TBG (blue dotted line) and BLG (grey dotted line, multiplied by a factor two) crystals from the same growth batch (full spectra are shown in Supplementary Note 2, Figure S2). We recall that the 2D peak of 30°-TBG is indistinguishable from that of MLG, apart from a blueshift attributable to the modified dielectric environment[21], which also applies to the MLG subsystem within TMBG.

Before discussing the results of electrical transport experiments, we discuss the expected spectral properties of electrically-biased TMBG, at zero and quantizing magnetic fields. This analysis is based on a self-consistent solution for charge and potential distribution in vertically biased few-layer graphene, taking into account the out-of-plane dielectric polarizability of each layer, using a model developed and tested in ref. 22. For TMBG in quantizing magnetic fields, the charge distribution is determined by the Landau-level (LL) pinning between its monolayer and bilayer components, stemming from the quantum-capacitance effect[22,43] (see Supplementary Note 3 and Fig. S3 for details). In this analysis we take into account proximity-induced energy shifts (δ) on the graphene layers interfacing encapsulating hBN, relative to the on-layer electrostatic potential of the middle one (interfacing carbon layers on both sides). Such energy shifts are in line with the recent model developed by Tseng and Chou for free-standing (i.e., interfaced with vacuum) small-angle TMBG[44]. While the actual magnitude of δ is not known (would depend on the encapsulating material), we find that it can be determined from the comparison of the computed (in)compressibility maps, Fig. 1g, h, with experimentally

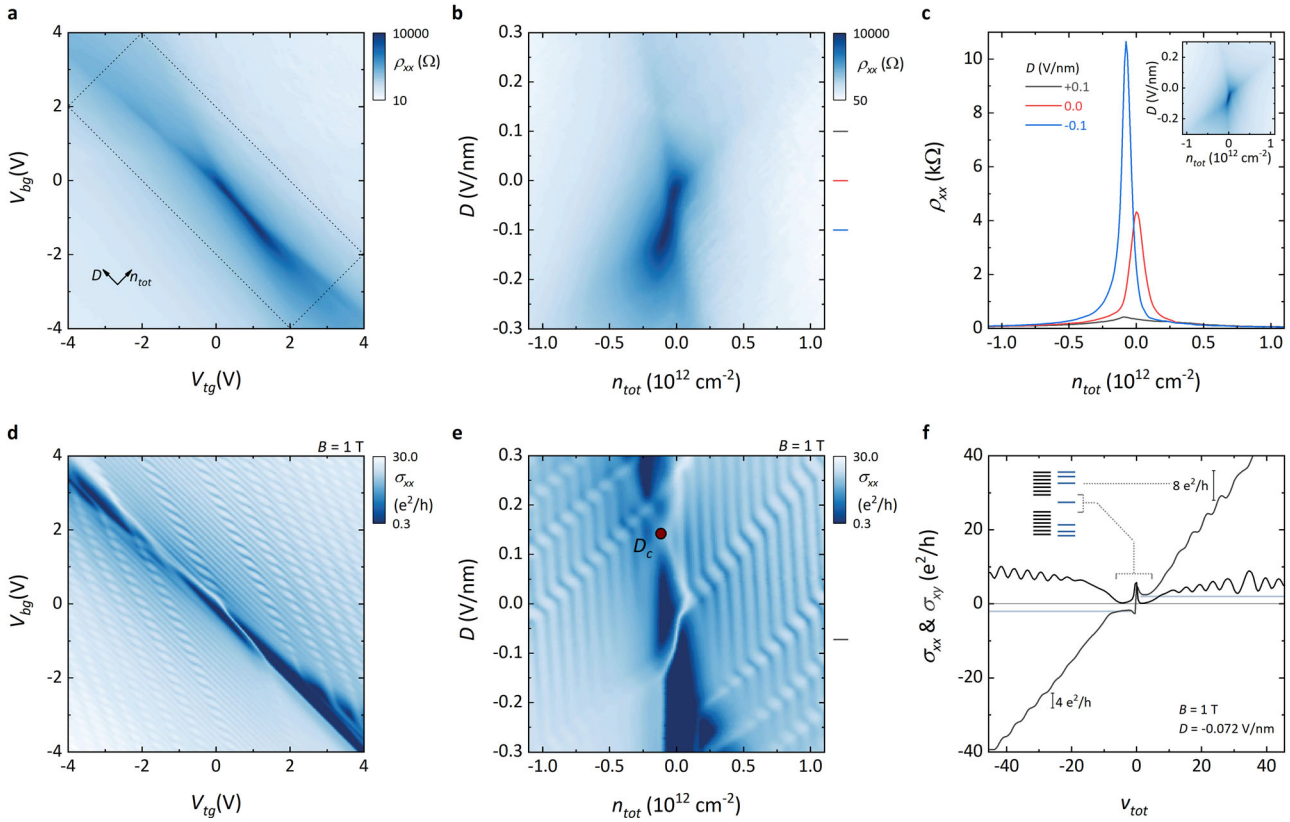

Fig. 2 | Low-temperature (magneto)transport of large-angle-twisted monolayer-bilayer graphene. a Longitudinal resistivity as a function of the gate potentials. **b** Longitudinal resistivity as a function of carrier density and displacement field, acquired within the dotted rectangle in panel (**a**). **c** Resistivity as a function of carrier density at selected displacement fields, as marked in (**b**). Inset: calculated resistivity of TMBG, as a function of carrier density and displacement field (the color scale is the same used in panel (**b**)). **d** Longitudinal conductivity at $B = 1$ T as a function of the gate potentials (same ranges as in (**a**)). **e** Longitudinal conductivity at $B = 1$ T, as a function of carrier density and displacement field (same ranges as in (**b**)). The dark red circle indicates the position of gap closing in BLG, which identifies the displacement field D_c compensating the intrinsic BLG polarization. **f** Longitudinal (black) and Hall (grey) conductivity as a function of the total filling factor $\nu_{tot} = n_{tot}h/eB$ at $D = -0.072$ V/nm at $B = 1$ T (see marker in panel (**e**)). The inset shows a sketch of the alignment of LLs from the two subsystems (blue for MLG, black for BLG). The MLG 0-LL lies within the BLG gap, leading to a MLG-like ± 2 e^2/h QH sequence at small fillings. 8 e^2/h steps in the Hall conductivity signal coincidence of LLs from the two subsystems (4 e^2/h steps are measured otherwise). All measurements are performed at $T = 0.36$ K on device D1. A logarithmic color scale is used in panels (**a**), (**b**), (**d**), (**e**).

measured quantum Hall (QH) maps in Fig. 2e. In Fig. 1g, h we plot the density of states (DOS) of TMBG as a function of n_{tot} and D for the cases of $\delta = 0$ and $\delta = 18$ meV, respectively. The color-coding is chosen to indicate when the chemical potential of electrons is pinned at the LLs (bright color) and when it crosses the inter-LL gaps (dark color). Diagonal (vertical) lines trace MLG (BLG) LLs, and their crossings correspond to mutual pinning of MLG and BLG LLs. The simulation of DOS maps was iterated for different values of δ, until best matching the experimental QH data.

The influence of proximity shift, δ, can be appreciated from the relative shift of compressibility maps in Fig. 1g, h. Its influence is also illustrated in Fig. 1f, where we plot the magnitude of the band gap in the BLG subsystem (Δ) as a function of D, self-consistently calculated for $\delta = 0$ (black line) and $\delta = 18$ meV (dark cyan line). In particular, the proximity shifts induce a finite Δ even in the absence of an external D-field. Furthermore, for each value of δ, one can identify a displacement field, D_c (see inset in Fig. 1f), that compensates the proximitized interlayer asymmetry and closes the BLG gap, suggesting a practical tool for precise measurements of the energy shift on graphene under different encapsulating environments.

In Fig. 2 we present gate-dependent electrical-transport measurements performed at $T = 0.36$ K on TMBG device D1 (analogous data from D2 are shown in Supplementary Note 4, Fig. S4). Figure 2a shows the longitudinal resistivity ρ_{xx} as a function of the top and bottom gate bias (V_{tg} and V_{bg}). At large carrier density (top right and bottom left corners), ρ_{xx} exhibits low values (<20 Ω) that indicate high carrier mobility, as typically observed in hBN-encapsulated graphene stacks. At low carrier density, we observe two intersecting features, with a region of high resistivity (ρ_{xx} up to ~10 kΩ) departing from $V_{tg} = V_{bg} = 0$ and extending only in the lower-right quadrant. To better discern the origin of the different transport contributions, in Fig. 2b we show ρ_{xx} data acquired within the dotted rectangle in Fig. 2a, as a function n_{tot} and D. Two split features, attributable to the charge neutrality points (CNPs) for the two subsystems, are visible. The first one, dispersing almost vertically along $n_{tot} = 0$, is associated to the subsystem with larger DOS, i.e., BLG. The second one, following a diagonal trajectory due to screening of the gate potentials by BLG, tracks the MLG CNP. We observe a marked slope change of the MLG CNP in the vicinity of $D = 0$ – signaling decreased screening and hence suppressed DOS in BLG – accompanied by large resistivity. At large negative D, the MLG CNP reverts to the original slope and, at the same time, resistivity is suppressed, indicating restored DOS in the BLG subsystem. This behavior is fully consistent with the MLG CNP crossing a band gap in BLG[33] and can be reproduced by calculations shown in Fig. 2c, inset (see Supplementary Note 3 for details). Overall, we notice the pronounced asymmetry with respect to the displacement field which reflects the structural asymmetry of TMBG (as opposed to measurements on structurally symmetric 30°-twisted MLG-BLG-MLG, shown in Supplementary Note 5, Fig. S5). This characteristic is highlighted by ρ_{xx} curves at selected D values, shown in Fig. 2c. At $D = 0$ we observe a clear

resistivity peak, which increases (and slightly shifts) at $D = -0.1$ V/nm; upon reversing displacement field ($D = +0.1$ V/nm), the resistivity peak disappears.

We then apply a moderate magnetic field ($B = 1$ T, Fig. 2d–f) perpendicular to the TMBG device, that reveals the independent Landau quantization of the two subsystems. In Fig. 2d, the longitudinal conductivity σ_{xx} (obtained by combining longitudinal and Hall resistivity data via the classical tensorial relation) shows two separated sets of oscillations, with different slope and frequency. The low-frequency oscillations are associated to the subsystem with smaller DOS, i.e., to MLG. The MLG oscillations show an uneven spacing, reflecting the energy separations between the LLs of massless Dirac Fermions, as previously observed in capacitively-coupled graphene layers, either spaced by dielectrics[45] or twisted by a large angle[23]. The high-frequency oscillations are associated to BLG and are absent in an extended region showing vanishing σ_{xx} (dark blue in Fig. 2d), which signals the BLG gap. Figure 2e (σ_{xx} as a function of n_{tot} and D) clearly shows that the gapped region collapses under a displacement field $D_c = 0.14$ V/nm (and reopens for $D > D_c$), which compensates the built-in BLG asymmetry. The measured pattern of LLs is best matched by DOS calculations shown in Fig. 1h, which include an energy shift $\delta = 18$ meV. The sign of D_c indicates that the intrinsic BLG polarization points from top to bottom, in accordance with ref. 44. Based on the magnitude of D_c, we estimate a corresponding BLG band gap $\Delta \sim 10$ meV, comparable to the one reported for TDBG[33,34]. Although spontaneous, few-meV gaps due to strong electron-electron interactions were measured in suspended BLG devices[46–48], those gaps show distinctive D-symmetric gap closing and reopening, ruling out a possible relation with the observed phenomenology. When the MLG zero-energy LL (0-LL) crosses the BLG gap, we clearly detect MLG-like QH states at filling factor $\nu_{tot} = \pm 2$, as shown by σ_{xx} and σ_{xy} curves in Fig. 2f. Outside of the BLG gap, we observe quantized steps in σ_{xy} with the expected amplitude 4 e^2/h (due to spin and valley degeneracy), with 8 e^2/h steps in case of coincidence of LLs from the two subsystems.

Having identified the experimental signatures expected for an intrinsic ~10 meV Bernal gap in dual-gated TMBG, we now proceed to its quantitative estimate. In Fig. 3a, we present isotherms of ρ_{xx} as a function of n_{tot}, measured at $D = -0.075$ V/nm on device D1 (analogous data from D2 are presented in Supplementary Note 6, Fig. S6). We observe thermal activation of the resistivity for $T < 100$ K, confirming the presence of an energy gap. This behavior is consistently observed at different D values, within the previously identified high-resistivity region (where the MLG CNP lies within the BLG gap). To appreciate changes in the conductivity of the BLG subsystem as a function of temperature, we minimize the conductivity contribution of the other subsystem, i.e. MLG, by considering the resistance maximum corresponding to MLG CNP. As shown in Fig. 3b, we find an Arrhenius-type dependence for the maximum of the resistivity peak $\rho_{xx}^{max} \propto \exp[\Delta/(2k_BT)]$ (where Δ is the band gap and k_B is the Boltzmann constant). The extracted gap reaches a maximum of $\Delta = 15$ meV at $D = -0.075$ V/nm, in line with calculations shown in Fig. 1f for $\delta = 18$ meV. The D-dependence shown Fig. 3b inset is influenced by MLG CNP crossing the BLG gap as a function of the gate voltages (see trajectory in Supplementary Fig. S3g), since the thermal activation gap reflects the distance between MLG CNP and the BLG band edges. As the displacement field becomes increasingly negative, the BLG gap widens (see Fig. 1f, dark cyan line), however MLG CNP approaches one of the BLG band edges, leading to a lower carrier activation energy and thus to a decrease of measured Δ. The band gap measured from thermal activation is finite even at $D = 0$, confirming that no external electric field is required for BLG gap opening within TMBG.

We further investigate the transport properties of TMBG under large perpendicular magnetic fields, which allows us to investigate the evolution of the multicomponent LLs of the two subsystems promoted by Coulomb interactions[49]. In Fig. 4a, b, we show σ_{xx} and σ_{xy} data at $B = 4$ T, as a function of ν_{tot} and D (the measurements span the usual n_{tot} and D ranges). For the MLG subsystem we observe only the 0-LL, which splits into four branches (bounding QH gaps at $\nu_{MLG} = 0, +1, -1$) due to complete lifting of the spin

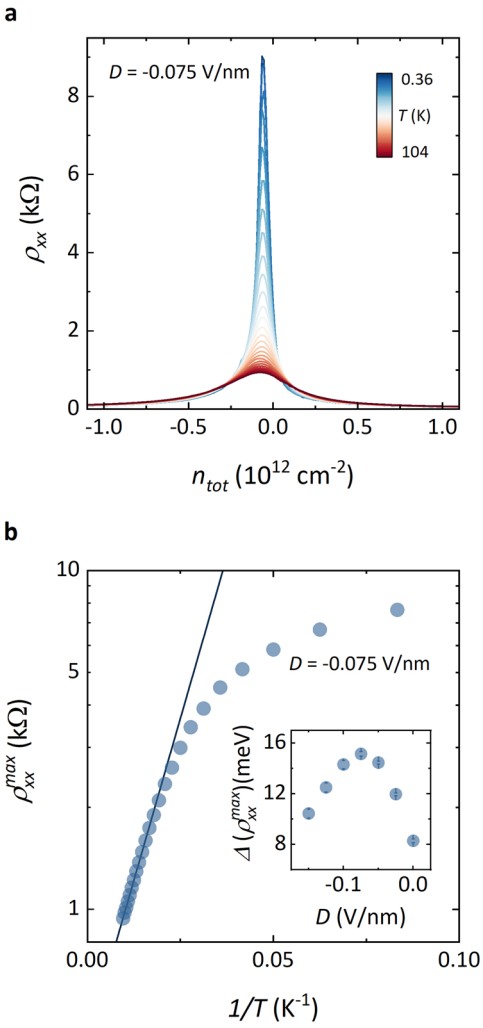

Fig. 3 | Thermal activation across the Bernal gap. a Longitudinal resistivity isotherms as a function of the carrier density, measured on sample D1 at $D = -0.075$ V/nm for 0.36 K < T < 104 K. **b** Arrhenius plot of the resistivity peak maxima from data in (**a**) (blue dots). The fit to $\rho_{xx}^{max} \propto \exp[\Delta/(2k_BT)]$ is shown as a blue continuous line. Inset: activation gaps obtained from the Arrhenius fit at different displacement fields. Error bars correspond to ± one standard error from the fits.

and valley degeneracy. The trajectories of the four MLG components are modulated by multiple crossings with LLs from the BLG subsystem, which also clearly show degeneracy lifting. In particular, the BLG 0-LL possesses an extra two-fold degeneracy associated with the orbital degree of freedom, making the multicomponent QH effect even richer and D-tunable[50]. We observe a clear symmetry of the BLG pattern with respect to the gap closing point at $D = D_c$, further confirming the intrinsic BLG polarization and its compensation by a positive displacement field. At $B = 8$ T (Fig. 4c, d) we observe multiple D-driven phase transitions in the BLG 0-LL around $D = D_c$, which reproduce recent results on BLG samples around $D = 0$[51]. These observations indicate that: (i) the quality of our CVD-based devices is fully comparable with samples based on mechanically exfoliated graphene layers; (ii) once the intrinsic polarization is compensated, the physics of the BLG subsystem embedded in TMBG is essentially indistinguishable from that of a stand-alone BLG. In Fig. 4e, f we show σ_{xx} and σ_{xy} curves at $B = 8$ T and selected values of displacement field. Figure 4e shows the full broken symmetry of the MLG 0-LL within the BLG band gap, while Fig. 4f highlights the full broken symmetry in of the BLG 0-LL (note that in this case the plateau sequence is shifted by a factor $-2e^2/h$ due to the contribution of two parallel-conducting edge channels from hole-doped MLG).

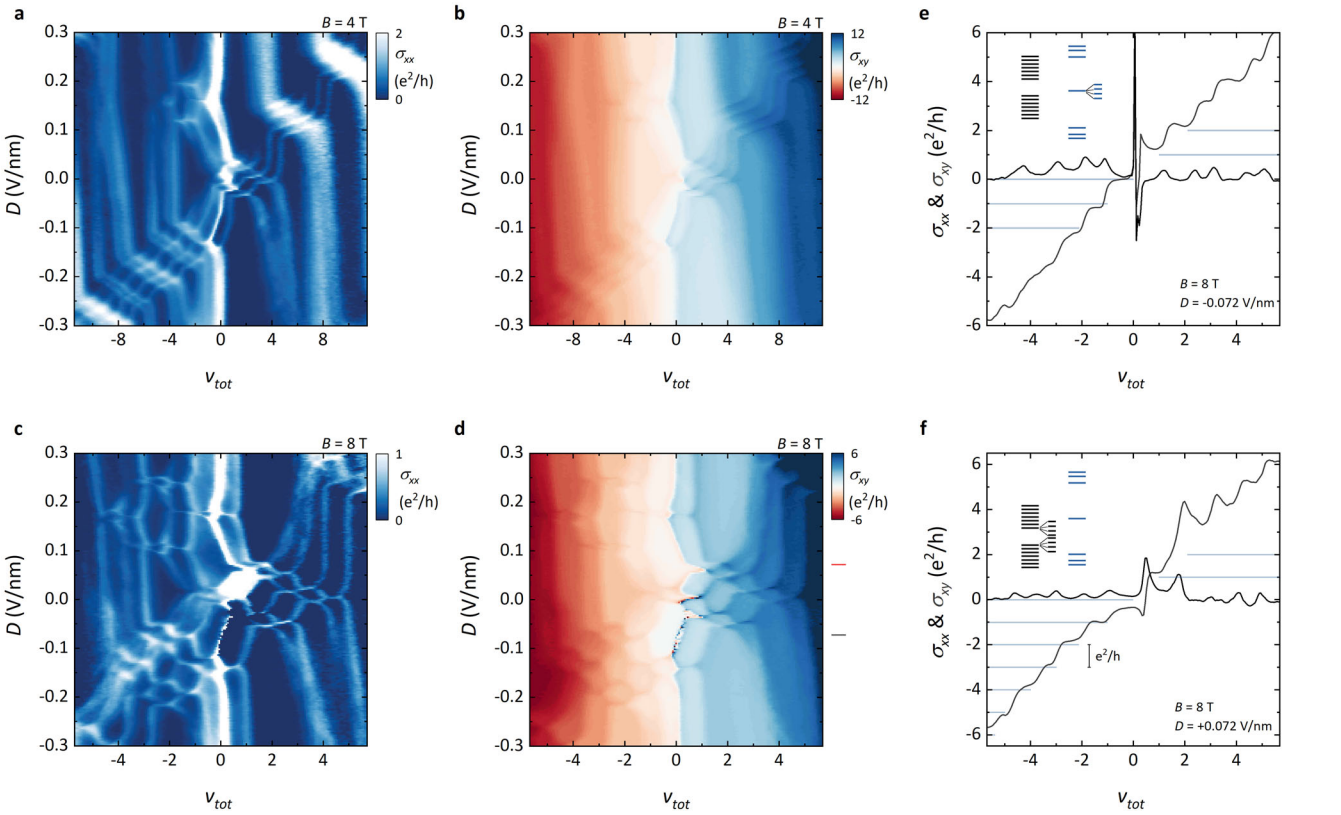

Fig. 4 | Multicomponent Landau levels in the two subsystems. Longitudinal and Hall conductivity measured on device D1 at $B = 4$ T (**a**, **b**) and $B = 8$ T (**c**, **d**). Curves at selected displacement field (indicated by the grey and red marks in panel (**d**)) are shown in (**e**) and (**f**), respectively; insets: sketches of the alignment of LLs from the two subsystems (blue for MLG, black for BLG), with degeneracy lifting in MLG (**e**) and BLG (**f**). Data acquired at $T = 0.36$ K on device D1.

Conclusions

In conclusion, we established the presence of a built-in BLG band gap in large-angle TMBG. The gap is induced by the lack of inversion symmetry, combined with proximity energy shifts on the outmost graphene layers. The BLG gap leads to specific signatures in electrical-transport properties, both under zero and quantizing magnetic fields that can be employed for its quantitative estimate. Analogous features have also been reported in a recent pre-print[52], where TMBG was obtained from exfoliated graphene flakes. Although our samples are encapsulated in hBN (as now ubiquitous in graphene research), we note that the observed effects are expected to occur also in free-standing TMBG, where even larger gaps are predicted[44], and in TMBG encapsulated with other dielectrics, which should modify the gap magnitude. Along this line, we can anticipate the use of TMBG and measurements of the BLG gap closing at D_c in dual-gated devices as a metrology platform for determining proximity-induced energy shifts caused by various encapsulating materials or insulating substrates (such as transition metal dichalcogenides). Moreover, the built-in BLG gap could be leveraged for broadband detection in the THz window (following recent findings on TDBG[34]), with tunable absorption properties depending on the encapsulating environment. Finally, let us remind the high interest in BLG gap for the definition of quantum point contacts[27] and dots[28,29], which might be designed with approaches beyond the current paradigm of local gating. The applicative potential of TMBG-based (opto)electronic and quantum devices is reinforced by the large-scale growth method employed in the fabrication of devices used in the reported studies.

Methods

Gate induced carrier density and displacement field

We adopt the relations $n_{tot} = 1/e$ x $(C_{tg}V_{tg}+C_{bg}V_{bg})$ and $D/\varepsilon_0 = (C_{bg}V_{bg}-C_{tg}V_{tg})/2$[18], where C_{bg} and C_{tg} are the capacitances per unit-area of the bottom and top gate, V_{bg} and V_{tg} are voltage bias applied to the bottom and top gate electrodes, e is the electron charge, ε_0 is the vacuum dielectric permittivity. Both the top and bottom hBN crystals used in the devices are ~30 nm thick (as determined by atomic force microscopy, AFM). We employ $\varepsilon_r = 3$ for the out-of plane dielectric constant of hBN[53,54], giving $C_{bg} = C_{tg} = 8.85 \times 10^{-8}$ Fcm^{-2}.

CVD growth of multilayer graphene with 0°/30° twist

TMBG crystals are grown by chemical vapor deposition in a Aixtron Black Magic reactor (Aixtron 4" BM-Pro) on electropolished Cu foil at a pressure of 25 mbar and a temperature of 1065 °C. After electropolishing, the Cu foil is heated in air on a hot plate at 250 °C for 15 min to oxidize the Cu surface. The Cu foil is then loaded in the CVD reactor and annealed in Ar atmosphere at 1065 °C for 10 mins, followed by 60 min of graphene growth in a mixture of Ar, H_2 and CH_4 with a flow ratio of 900:40:0.8 sccm, respectively. Then the CVD reactor is cooled down to 100 °C in an Ar atmosphere. After growth, the shape of graphene crystals shows a deviation from perfect hexagons due to diffusion-limited growth mechanisms, as typical for oxygen-rich Cu foil[55] and low partial pressure of H_2[56]. Crystals obtained under these conditions show regular electron diffraction patterns[21] and low strain[57] (< 1% after transfer to SiO_2/Si; though strain influences details of the BLG dispersion, the system is expected to remain gapless at such values[58]). We observe concentric multilayers with different interlayer rotations, each one locked to either 0° or 30° (with a preponderance of aligned layers, attesting at ~60–70%). Among the trilayer crystals, a ~ 30% fraction shows the stacking configuration targeted for this study.

vdW assembly and device fabrication

Before vdW assembly, CVD-grown TMBG crystals are transferred to a SiO_2/Si substrate using a semi-dry technique involving electrochemical delamination with a PMMA/PPC carrier membrane[57]. We first prepare a crystalline bottom gate by picking-up a graphite flake (~5 nm thick) using

an hBN flake carried by a PC/PDMS stamp[59]. The graphite back-gate screens disorder from the underlying SiO_2, yielding clean transport properties in gapped BLG devices[60]. After release and cleaning in chloroform, we use contact-mode AFM to mechanically clean the hBN surface[61]. A second hBN flake is used to pick-up a portion of the TMBG crystal. The hBN/TMBG is subsequently released at 180 °C on top of the cleaned hBN/graphite. The devices are processed combining electron-beam lithography, reactive ion etching and thermal evaporation of Cr/Au edge contacts and top-gates.

Raman spectroscopy

A commercial Renishaw "InVia" system is used for Raman characterization. Spectra are acquired employing a 532 nm wavelength and with a 100x objective, producing a fluence ~350 μW/ μm^2 on the sample, using a 1800 l/mm grating. Calibration of the system is performed using the Si Raman peak at 520 cm^{-1}.

Electrical transport measurements

The electrical transport measurements are performed in a dry "ICE 300 mK He-3 Continuos" cryostat equipped with an 8 T superconducting magnet (sample D1) and in a dry "ICE 3 K INV" cryostat (sample D2). Four-probe measurements are performed with low-frequency (~13 Hz) lock-in detection, either in a constant current (~100 nA), or constant voltage configuration (0.1 mV). The source-drain current and longitudinal and Hall voltage drops are simultaneously recorded, while biasing the top and bottom gates using a dc source-meter.

Data availability

The data presented in this study are available at https://doi.org/10.5281/zenodo.14178601.

Received: 25 July 2024; Accepted: 22 November 2024;
Published online: 01 December 2024

References

1. Castro Neto, A. H., Guinea, F., Peres, N. M. R., Novoselov, K. S. & Geim, A. K. The Electronic Properties of Graphene. *Rev. Mod. Phys.* **81**, 109–162 (2009).
2. Slizovskiy, S., McCann, E., Koshino, M. & Fal'ko, V. I. Films of Rhombohedral Graphite as Two-Dimensional Topological Semimetals. *Commun. Phys.* **2**, 1–10 (2019).
3. Garcia-Ruiz, A., Slizovskiy, S. & Fal'ko, V. I. Flat Bands for Electrons in Rhombohedral Graphene Multilayers with a Twin Boundary. *Adv. Mater. Interfaces* **10**, 2202221 (2023).
4. Garcia-Ruiz, A., Enaldiev, V., McEllistrim, A. & Fal'ko, V. I. Mixed-Stacking Few-Layer Graphene as an Elemental Weak Ferroelectric Material. *Nano Lett.* **23**, 4120–4125 (2023).
5. McCann, E. & Fal'ko, V. I. Landau-Level Degeneracy and Quantum Hall Effect in a Graphite Bilayer. *Phys. Rev. Lett.* **96**, 086805 (2006).
6. Ge, Z. et al. Control of Giant Topological Magnetic Moment and Valley Splitting in Trilayer Graphene. *Phys. Rev. Lett.* **127**, 136402 (2021).
7. Carr, S. et al. Twistronics: Manipulating the Electronic Properties of Two-Dimensional Layered Structures through Their Twist Angle. *Phys. Rev. B* **95**, 075420 (2017).
8. Bistritzer, R. & MacDonald, A. H. Moiré Bands in Twisted Double-Layer Graphene. *Proc. Natl. Acad. Sci.* **108**, 12233–12237 (2011).
9. Cao, Y. et al. Correlated Insulator Behaviour at Half-Filling in Magic-Angle Graphene Superlattices. *Nature* **556**, 80–84 (2018).
10. Cao, Y. et al. Unconventional Superconductivity in Magic-Angle Graphene Superlattices. *Nature* **556**, 43–50 (2018).
11. Andrei, E. Y. et al. The Marvels of Moiré Materials. *Nat. Rev. Mater.* **6**, 201–206 (2021).
12. Chen, S. et al. Electrically Tunable Correlated and Topological States in Twisted Monolayer–Bilayer Graphene. *Nat. Phys.* **17**, 374–380 (2021).
13. Xu, S. et al. Tunable van Hove Singularities and Correlated States in Twisted Monolayer–Bilayer Graphene. *Nat. Phys.* **17**, 619–626 (2021).
14. Polshyn, H. et al. Electrical Switching of Magnetic Order in an Orbital Chern Insulator. *Nature* **588**, 66–70 (2020).
15. He, M. et al. Competing Correlated States and Abundant Orbital Magnetism in Twisted Monolayer-Bilayer Graphene. *Nat. Commun.* **12**, 4727 (2021).
16. Zhang, C. et al. Local Spectroscopy of a Gate-Switchable Moiré Quantum Anomalous Hall Insulator. *Nat. Commun.* **14**, 3595 (2023).
17. Polshyn, H. et al. Topological Charge Density Waves at Half-Integer Filling of a Moiré Superlattice. *Nat. Phys.* **18**, 42–47 (2022).
18. Sanchez-Yamagishi, J. D. et al. Quantum Hall Effect, Screening, and Layer-Polarized Insulating States in Twisted Bilayer Graphene. *Phys. Rev. Lett.* **108**, 076601 (2012).
19. Sanchez-Yamagishi, J. D. et al. Helical Edge States and Fractional Quantum Hall Effect in a Graphene Electron–Hole Bilayer. *Nat. Nanotech* **12**, 118–122 (2017).
20. Rickhaus, P. et al. The Electronic Thickness of Graphene. *Sci. Adv.* **6**, eaay8409 (2020).
21. Pezzini, S. et al. 30°-Twisted Bilayer Graphene Quasicrystals from Chemical Vapor Deposition. *Nano Lett.* **20**, 3313–3319 (2020).
22. Slizovskiy, S. et al. Out-of-Plane Dielectric Susceptibility of Graphene in Twistronic and Bernal Bilayers. *Nano Lett.* **21**, 6678–6683 (2021).
23. Piccinini, G. et al. Parallel Transport and Layer-Resolved Thermodynamic Measurements in Twisted Bilayer Graphene. *Phys. Rev. B* **104**, L241410 (2021).
24. McCann, E. Asymmetry Gap in the Electronic Band Structure of Bilayer Graphene. *Phys. Rev. B* **74**, 161403 (2006).
25. Oostinga, J. B., Heersche, H. B., Liu, X., Morpurgo, A. F. & Vandersypen, L. M. K. Gate-Induced Insulating State in Bilayer Graphene Devices. *Nat. Mater.* **7**, 151–157 (2008).
26. Zhang, Y. et al. Direct Observation of a Widely Tunable Bandgap in Bilayer Graphene. *Nature* **459**, 820–823 (2009).
27. Overweg, H. et al. Electrostatically Induced Quantum Point Contacts in Bilayer Graphene. *Nano Lett.* **18**, 553–559 (2018).
28. Banszerus, L. et al. Gate-Defined Electron–Hole Double Dots in Bilayer Graphene. *Nano Lett.* **18**, 4785–4790 (2018).
29. Eich, M. et al. Coupled Quantum Dots in Bilayer Graphene. *Nano Lett.* **18**, 5042–5048 (2018).
30. Zhou, H. et al. Isospin Magnetism and Spin-Polarized Superconductivity in Bernal Bilayer Graphene. *Science* **375**, 774–778 (2022).
31. de la Barrera, S. C. et al. Cascade of Isospin Phase Transitions in Bernal-Stacked Bilayer Graphene at Zero Magnetic Field. *Nat. Phys.* **18**, 771–775 (2022).
32. Seiler, A. M. et al. Quantum Cascade of Correlated Phases in Trigonally Warped Bilayer Graphene. *Nature* **608**, 298–302 (2022).
33. Rickhaus, P. et al. Gap Opening in Twisted Double Bilayer Graphene by Crystal Fields. *Nano Lett.* **19**, 8821–8828 (2019).
34. Agarwal, H. et al Ultra-Broadband Photoconductivity in Twisted Graphene Heterostructures with Large Responsivity. *Nat. Photon.* 1–7, https://doi.org/10.1038/s41566-023-01291-0 (2023).
35. Zhang, Z. et al. Growth and Applications of Two-Dimensional Single Crystals. *2D Mater.* **10**, 032001 (2023).
36. Ahn, S. J. et al. Dirac Electrons in a Dodecagonal Graphene Quasicrystal. *Science* **361**, 782–786 (2018).
37. Moon, P., Koshino, M. & Son, Y.-W. Quasicrystalline Electronic States in 30° Rotated Twisted Bilayer Graphene. *Phys. Rev. B* **99**, 165430 (2019).
38. Yan, Z. et al. Large Hexagonal Bi- and Trilayer Graphene Single Crystals with Varied Interlayer Rotations. *Angew. Chem. Int. Ed.* **53**, 1565–1569 (2014).
39. Kim, K. et al. Van Der Waals Heterostructures with High Accuracy Rotational Alignment. *Nano Lett.* **16**, 1989–1995 (2016).
40. Cao, Y. et al. Superlattice-Induced Insulating States and Valley-Protected Orbits in Twisted Bilayer Graphene. *Phys. Rev. Lett.* **117**, 116804 (2016).

41. Suárez Morell, E., Pacheco, M., Chico, L. & Brey, L. Electronic Properties of Twisted Trilayer Graphene. *Phys. Rev. B* **87**, 125414 (2013).
42. Ferrari, A. C. et al. Raman Spectrum of Graphene and Graphene Layers. *Phys. Rev. Lett.* **97**, 187401 (2006).
43. Ando, T., Fowler, A. B. & Stern, F. Electronic Properties of Two-Dimensional Systems. *Rev. Mod. Phys.* **54**, 437–672 (1982).
44. Tseng, W.-E., Chou, M.-Y. Electrically Tunable Flat Bands with Layer-Resolved Charge Distribution in Twisted Monolayer-Bilayer Graphene. arXiv December 4, https://doi.org/10.48550/arXiv.2312.01820 (2023).
45. Kim, S. et al. Direct Measurement of the Fermi Energy in Graphene Using a Double-Layer Heterostructure. *Phys. Rev. Lett.* **108**, 116404 (2012).
46. Weitz, R. T., Allen, M. T., Feldman, B. E., Martin, J. & Yacoby, A. Broken-Symmetry States in Doubly Gated Suspended Bilayer Graphene. *Science* **330**, 812–816 (2010).
47. Velasco, J. et al. Transport Spectroscopy of Symmetry-Broken Insulating States in Bilayer Graphene. *Nat. Nanotech* **7**, 156–160 (2012).
48. Freitag, F., Trbovic, J., Weiss, M. & Schönenberger, C. Spontaneously Gapped Ground State in Suspended Bilayer Graphene. *Phys. Rev. Lett.* **108**, 076602 (2012).
49. Young, A. F. et al. Spin and Valley Quantum Hall Ferromagnetism in Graphene. *Nat. Phys.* **8**, 550–556 (2012).
50. Lee, K. et al. Chemical Potential and Quantum Hall Ferromagnetism in Bilayer Graphene. *Science* **345**, 58–61 (2014).
51. Xiang, F. et al. Intra-Zero-Energy Landau Level Crossings in Bilayer Graphene at High Electric Fields. *Nano Lett.* **23**, 9683–9689 (2023).
52. Jiang, J. et al. Featuring Nuanced Electronic Band Structure in Gapped Multilayer Graphene. arXiv https://doi.org/10.48550/arXiv.2405.12885 (2024).
53. Yang, F. et al. Experimental Determination of the Energy per Particle in Partially Filled Landau Levels. *Phys. Rev. Lett.* **126**, 156802 (2021).
54. Ferreira, F., Enaldiev, V. V. & Fal'ko, V. I. Scaleability of Dielectric Susceptibility ε_{zz} with the Number of Layers and Additivity of Ferroelectric Polarization in van Der Waals Semiconductors. *Phys. Rev. B* **106**, 125408 (2022).
55. Hao, Y. et al. The Role of Surface Oxygen in the Growth of Large Single-Crystal Graphene on Copper. *Science* **342**, 720–723 (2013).
56. Wu, B. et al. Self-Organized Graphene Crystal Patterns. *NPG Asia Mater.* **5**, e36 (2013).
57. Giambra, M. A. et al. Wafer-Scale Integration of Graphene-Based Photonic Devices. *ACS Nano* **15**, 3171–3187 (2021).
58. Mucha-Kruczyński, M., Aleiner, I. L. & Fal'ko, V. I. Strained Bilayer Graphene: Band Structure Topology and Landau Level Spectrum. *Phys. Rev. B* **84**, 041404 (2011).
59. Purdie, D. G. et al. Cleaning Interfaces in Layered Materials Heterostructures. *Nat. Commun.* **9**, 5387 (2018).
60. Icking, E. et al. Transport Spectroscopy of Ultraclean Tunable Band Gaps in Bilayer Graphene. *Adv. Electron. Mater.* **8**, 2200510 (2022).
61. Goossens, A. M. et al. Mechanical Cleaning of Graphene. *Appl. Phys. Lett.* **100**, 073110 (2012).

Acknowledgements

This work has received funding from: PNRR MUR project PE00000023 – NQSTI and the European Union's Horizon 2020 Research and Innovation Programme under Grant Agreement No. 881603 Graphene Flagship. We acknowledge funding from the European Union through the GraPh-X project (Grant agreement ID: 101070482). K.W. and T.T. acknowledge support from the JSPS KAKENHI (Grant Numbers 21H05233 and 23H02052), the CREST (JPMJCR24A5), JST and World Premier International Research Center Initiative (WPI), MEXT, Japan. V.F. and S.S. acknowledge support from EPSRC grant EP/V007033/1, British Council and International Science Partnerships Fund Grant 1185409051 for Research Collaboration between UK and Japan.

Author contributions

S.P. conceived and designed the experiments. Z.M.G. and V.M. synthesized the TMBG crystals and transferred them to SiO_2/Si. A.B. and S.P. fabricated the devices and performed the transport measurements. A.B. and S.P. performed the data analysis, with support from A.R. and S.F. S.S. and V.I.F. performed the theoretical modelling. K.W. and T.T. provided hexagonal boron nitride crystals. F.B. and C.C. supported the experiments and coordinated the collaboration together with V.I.F and S.P. A.B. and S.P. co-wrote the manuscript with input from all co-authors.

Competing interests

The authors declare no competing interests.

Additional information

Supplementary information The online version contains supplementary material available at https://doi.org/10.1038/s42005-024-01887-0.

Correspondence and requests for materials should be addressed to Camilla Coletti or Sergio Pezzini.

Peer review information *Communications Physics* thanks Julien Barrier and the other, anonymous, reviewer(s) for their contribution to the peer review of this work.

Reprints and permissions information is available at http://www.nature.com/reprints

Publisher's note Springer Nature remains neutral with regard to jurisdictional claims in published maps and institutional affiliations.

Open Access This article is licensed under a Creative Commons Attribution 4.0 International License, which permits use, sharing, adaptation, distribution and reproduction in any medium or format, as long as you give appropriate credit to the original author(s) and the source, provide a link to the Creative Commons licence, and indicate if changes were made. The images or other third party material in this article are included in the article's Creative Commons licence, unless indicated otherwise in a credit line to the material. If material is not included in the article's Creative Commons licence and your intended use is not permitted by statutory regulation or exceeds the permitted use, you will need to obtain permission directly from the copyright holder. To view a copy of this licence, visit http://creativecommons.org/licenses/by/4.0/.

© The Author(s) 2024